




Article

# Flexural Behaviour of Foam Cored Sandwich Structures with Through-Thickness Reinforcements

Ghilané Bragagnolo <sup>1,2</sup>, Andrew D. Crocombe <sup>1</sup>, Stephen L. Ogin <sup>1</sup>, Alessandro Sordon <sup>2</sup>  
and Iman Mohagheghian <sup>1,\*</sup> 

<sup>1</sup> Department of Mechanical Engineering Sciences, University of Surrey, Surrey, Guildford GU2 7XH, UK

<sup>2</sup> McLaren Automotive Ltd., Woking, Surrey GU21 4YH, UK

\* Correspondence: i.mohagheghian@surrey.ac.uk

**Abstract:** Composite sandwich structures are well-suited for applications requiring high bending strength, flexural rigidity, crashworthiness, and light weight. However, skin–core debonding and core failure remain a barrier to optimal structural performance when polymeric foams are used as core materials. Suppressing or compartmentalising these failure modes can enhance the structural integrity of sandwich structures. In this paper, the flexural response of a sandwich structure was improved by adding carbon fibre-reinforced plastic in the form of through-thickness ribs during the manufacturing process. The effect of the position of the ribs was investigated using a quasi-static three-point bend test. A camera was used to capture failure events, while the digital image correlation technique provided the full-strain field at different stages of loading. Improved flexural performance was obtained when a reinforcement was placed on either side of the loading roller. With this configuration, skin–core debonding was restricted to a confined portion of the panel, resulting in a more localised and stable fracture process, which involved enhanced foam crushing and hardening. A simple FEA approach has been adopted in this paper and has proven to be an effective approach for capturing the details of the failure process, including the debonding in the composite foam structures, without the need for complex and computationally expensive interface modelling.

**Keywords:** sandwich structures; three-point bending; foam core; finite element model; DIC



**Citation:** Bragagnolo, G.; Crocombe, A.D.; Ogin, S.L.; Sordon, A.; Mohagheghian, I. Flexural Behaviour of Foam Cored Sandwich Structures with Through-Thickness Reinforcements. *J. Compos. Sci.* **2023**, *7*, 125. <https://doi.org/10.3390/jcs7030125>

Academic Editor: Francesco Tornabene

Received: 28 February 2023

Accepted: 13 March 2023

Published: 16 March 2023



**Copyright:** © 2023 by the authors. Licensee MDPI, Basel, Switzerland. This article is an open access article distributed under the terms and conditions of the Creative Commons Attribution (CC BY) license (<https://creativecommons.org/licenses/by/4.0/>).

## 1. Introduction

Composite sandwich structures are increasingly gaining interest from car manufacturers as a consequence of their higher stiffness-to-weight ratio and superior crashworthiness capabilities, compared to conventional metallic structures [1]. Moreover, decreasing vehicle weight, in order to improve efficiency without compromising performance, is becoming more and more important as the need to reduce emissions increases. However, due to the significant mismatch in material properties, the skin–core interfaces are weak points within sandwich components, and once debonding occurs, the load-carrying capacity of a sandwich structure is severely compromised [2]. As a result, much effort has been focused in the literature on improving skin/core adhesion, to avoid debonding and to maintain the integrity of the sandwich structure. In particular, Pfund [3] explained the importance of the preparation of the adherend surfaces prior to adhesion, especially when polymeric foams are used as core materials. Hamada et al. [4] also demonstrated the difference in progressive crushing behaviour as a consequence of using different surface treatments for the adherends. Skin–core interface performance was also seen to be affected by core material properties [5], core thickness [6], and interlaminar toughening techniques, such as using toughened resin, through-thickness stitching, thermoplastic resin additives, and thermoplastic interleaves [7]. Incorporation of nanomaterials has also been shown to enhance the skin–core interfacial fracture toughness [8]. Mamalis et al. [9,10] suggested including localised reinforcements in the form of FRP tubes and corrugations penetrating

through the core and linking the external skins with the aim of providing a number of skin-to-skin connection points for effective load transfer, even in the event of skin–core debonding. More recently, Henao et al. [11], Jishi et al. [12], and Blok et al. [13] studied the effect of adding through-thickness reinforcements in the form of tufting and stitching. Henao et al. [11] obtained an increase in the edgewise compression strength and in the energy absorption when tufted through-thickness reinforcements were added to the sandwich panels to restrict skin–core interface failure. Jishi et al. [12] and Blok et al. [13] used through-thickness glass and aramid fibre tufts, respectively, to reinforce sandwich structures. The results showed an increase in the skin–core interfacial fracture toughness and the energy absorption capability of the structure, due to an improved skin-to-core adhesion, which triggered a more stable and localised fracture of the skins.

Numerical modelling has also been used to investigate the behaviour of sandwich panels under various loading conditions, including both static and dynamic loadings. Appropriate modelling of debonding process is key to the accurate prediction of the structural integrity of sandwich structures. Typically, two main methods have been employed in the literature, the virtual crack closure technique (VCCT) and cohesive zone modelling (CZM). Glaessgen et al. [14] used VCCT for investigating the debonding failure of a sandwich-composite cryogenic fuel tank with internal core pressure. Toygar et al. [15] and Balaban and Tee [16] also utilised VCCT for numerical modelling the fracture behaviour of sandwich structure composite beams under three-point bending. The main advantages of using VCCT are that the bond fracture toughness is the only input parameter needed to define the interface behaviour, and it uses a surface-based framework to model crack propagation; hence, additional elements are not required. However, prior knowledge of the crack location and the propagation path are required when using VCCT. These shortcomings can be overcome by using CZM for the cases where crack initiation and propagation need to be modelled from initially uncracked surfaces. Xie et al. [17] utilised CZM in modelling the flexural behaviour of web-reinforced GFRP-PET foam sandwich under quasi-static four-point bending. Their results indicated that the GFRP webs can effectively prevent catastrophic failure of the sandwich structure. The numerical model was capable of the accurate prediction of post-failure behaviour. Chen et al. [18] investigated the influence of through-thickness reinforcement pins on the low-velocity impact performance of foam core sandwich structures. They also employed CZM in their modelling. The influence of the relative size and location of reinforcement pins, with respect to that of the impactor on the contact force, damage resistance, indentation depth, and perforation threshold energy, were studied. The results indicated that the deformation and damage patterns are significantly influenced by the reinforcement. Ghimire and Chen [19] used an extended CZM model to study the geometrical ratio effects on failure mechanisms of functionally graded sandwiches with multi-layered cores. The failure load was increased by increasing the geometrical depth-span ratio. The main drawback of CZM is that the approach is computationally expensive because it involves introducing cohesive elements to the model for which the accuracy of the predictions depends on a number of input parameters (i.e., to define damage law) and on the size of elements (often a very fine mesh is required).

In this work, core webs were manufactured for investigation by wrapping foam blocks with carbon fibre plies prior to resin infusion, in order to easily and efficiently create through-thickness reinforcements within flat sandwich panels. When designing for sandwich panels, especially in the automotive industry, it is possible to anticipate where the localised loadings are most likely to happen, either in the form of static or dynamic loading (e.g., impact). In this paper, quasi-static three-point bend tests were carried out on three different rib reinforcements, and the responses were compared in terms of the initial failure (i.e., the maximum load) and the post-maximum load behaviour. The three structures exhibited considerable load carrying capacity beyond the initial failure point with the extent of this capacity depending on the location of the ribs. This difference in behaviour, beyond the initial failure point, can have a significant impact on the structural integrity (in the case of accidental indentation) or on the energy absorption capability of the structure

(in the case of crash). Rib placement can have a strong influence in compartmentalising the damage and enhancing the structural integrity as a result. The experimental results have been compared to FE predictions where a foam failure criterion has been included to model both core failure and skin–core debonding with the aim of significantly reducing the extensive computational time required when interfacial failure techniques, such as cohesive zone modelling (CZM) and virtual crack closure technique (VCCT), are used. The modelling approach can be developed to investigate other loading configurations.

## 2. Materials and Methods

### 2.1. Materials

The skins of the sandwich panels consisted of CFRP laminates, including layers of both unidirectional (UD) and non-crimped fabric (NCF) biaxial (BIAX) plies. Table 1 includes the material properties of both materials. Measurement of skin material properties followed the relevant ASTM guidelines (i.e., uniaxial tension (ASTM D3039 [20]), compression (ASTM D3410 [21]), cyclic shear (ASTM D3518 [22])). A polymeric cellular foam was used as core material for the sandwich panels; its mechanical properties are given in Table 2 [23].

**Table 1.** Material properties for the CFRP skin material. For the UD ply, 1 is the direction of the fibres and 2 is the direction perpendicular to the fibres.

	Young's Modulus		Poisson's Ratio	Density	Shear Modulus	Compressive Strength		Tensile Strength		Shear Strength
	$E_{11}$ [GPa]	$E_{22}$ [GPa]	$\nu_{12}$	$\rho$ [kg/m <sup>3</sup> ]	$G_{12} = G_{13} = G_{23}$ [GPa]	$X_{11}$ [MPa]	$X_{22}$ [MPa]	$X_{t11}$ [MPa]	$X_{t22}$ [MPa]	S [MPa]
UD	127	8	0.3	1500	6.1	656	169	1926	29	34
BIAX	65	66	0.03	1500	2.4	585	585	1005	1005	22

**Table 2.** Foam core material properties [23].

	Tensile Elastic Modulus	Compressive Elastic Modulus	Density	Tensile Strength	Compressive Yield Strength	Shear Yield Strength
	$E_T$ [MPa]	$E_C$ [MPa]	$\rho$ [kg/m <sup>3</sup> ]	$X_T$ [MPa]	$X_C$ [MPa]	$X_S$ [MPa]
FOAM CORE	143	123	110	2	1.9	1.5

Flat sandwich panels were manufactured using resin infusion moulding (RTM), and rectangular specimens were cut using a diamond blade saw, according to the dimensions defined by ASTM C393 [24]. This particular standard was followed as it proposes guidelines for determining core properties of flat panels under flexural loading. Images of the three specimen configurations considered are shown in Figure 1 (detailed dimensions are provided in Section 2.2).

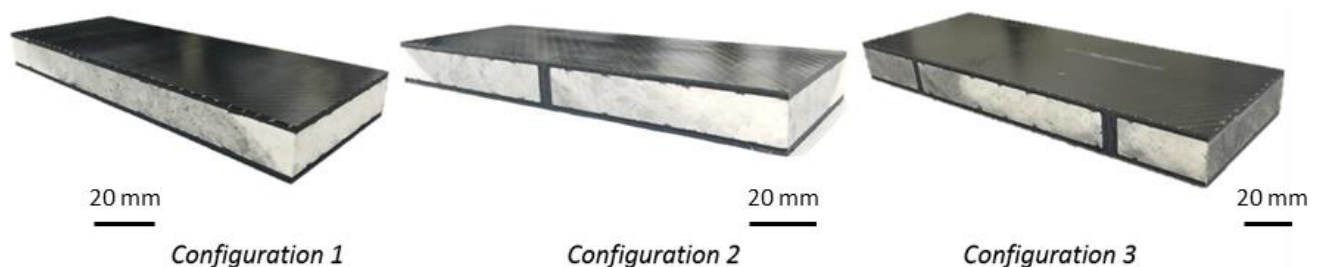


**Figure 1.** Images of the three specimen configurations considered.

Configuration 1 did not include any CFRP through-thickness reinforcement (rib). Configuration 2 included one rib at the mid-length of the specimen, and the third configuration included two ribs located at 40 mm from either end of the specimens. The panels were fabricated by co-curing the skins and the ribs to the foam core during the RTM process. In particular, prior to the infusion stage, the 15 mm thick core was divided into strips 105 mm long by 75 mm wide, and each strip was wrapped with four dry carbon fibre plies to produce the through-thickness ribs and the inner layers of the top and bottom skins. Three plies of carbon fibre were then stacked on the top and the bottom of the wrapped core strips to create the external layers of the skins. Figure 2 shows a schematic of the stacking sequence used during the manufacturing process.

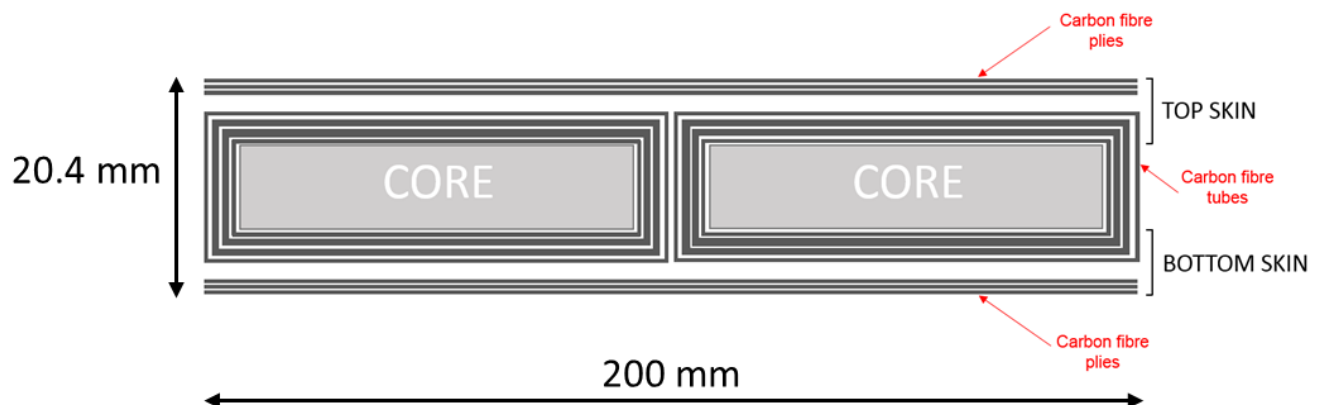


**Figure 2.** Schematic of the stacking sequence of the floor panel; foam strips, 4 CFRP plies wrapped around each foam strips, and 3 CFRP plies placed on top and bottom of the wrapped foam strips. Each skin was then made of 7 CFRP plies, and each rib was made of 8 CFRP plies.

## 2.2. Test Methods

Three-point bending mechanical tests were conducted on the sandwich specimens on an Instron screw-driven testing machine, with loading and supporting rollers consisting of 25 mm diameter steel cylinders. The test speed for cross-head displacement was 6 mm/min, as suggested in ASTM C393 [24], and the cross-head displacement of the loading roller, as well as the reaction force, were recorded throughout the experiment. For each configuration, at least two tests were performed to ensure the repeatability of the results.

A schematic of the test configuration is shown in Figure 3, and Table 3 shows the dimensions of the specimens. Three specimens of each configuration were tested: one specimen for each configuration was tested with a camera positioned in front of the testing machine to capture the failure process, while the other two specimens were tested with DIC equipment to map the evolution of the full-strain field on the specimen edge face. The 3D-DIC system was supplied by Correlated Solutions Inc. and included two 9-megapixel cameras and Vic-3D software for post-processing and analysis of the images. In order to use the DIC technique, an initial thin uniform layer of white paint was applied to the edge of the sample by spray painting. Once this first layer was dry, a random black speckle pattern was sprayed on top of the white layer to produce a speckle pattern with adequate contrast.

**Table 3.** Three-point bending test specimen dimensions.

2L [mm]	S [mm]	B [mm]	$h_c$ [mm]	$h_f$ [mm]
200	150	75	15	2.7

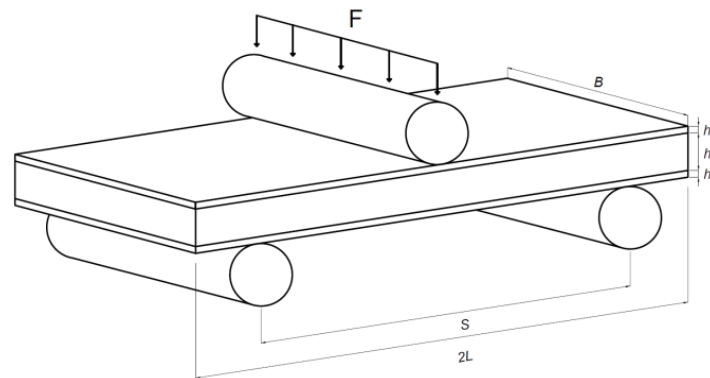


**Figure 3.** Three-point bending test configuration.

### 3. Finite Element Analysis

The 3D FE models of the sandwich panels under three-point bending loading were constructed using the software Abaqus/Explicit (Abaqus 2017). Here, we use a dynamic solver to analyse a quasi-static problem, as it is a more efficient tool for problems involving non-linear deformation and contact between various parts. The geometry and dimensions of the modelled sandwich beams with ‘Configuration 1’, ‘Configuration 2’, and ‘Configuration 3’ were the same as the experimental specimens described in the previous section (Figure 3 and Table 3). Similarly, the boundary conditions used in the FEM reproduced the experimental conditions.

In the models, each skin was partitioned through the thickness to represent each composite ply with a layer of elements and was meshed using continuum shell SC8R elements. The foam core was meshed using C3D8R solid elements and was modelled using the crushable foam plasticity material model [25]. To include the prediction of foam failure, the foam failure criterion proposed by [26,27] was implemented as a VUSDFLD user subroutine. This failure criterion, developed using invariant theory, needs only three parameters to describe the failure envelope in the 3-D stress space [5], and the parameters used for calibrating the failure model are the same as those described in our previous publication [5]. The model was used to predict both foam failure (in tension, compression, and shear) and skin–core debonding. The loading and support rollers were modelled as “analytical” rigid bodies and, while the reference points of the support rollers were fixed, a constant velocity of 1500 mm/s was applied to the reference point of the loading roller. To simulate the quasi-static problems in Abaqus Explicit, it is a common practice to use an artificially high loading speed, in order to save computational time. To check that the inertia is not playing a significant role in the outcome, kinetic energy is compared against total strain energy. If this value is below 5%, the dynamic effects can be considered small. Such an approach was taken in this case.

General contact, with a tangential friction coefficient of 0.2, was used to define the interaction between the specimen and the rollers and to prevent penetration between the different parts of the model (skins, core, ribs, and rollers). The two composite skins and the CFRP ribs were meshed with one element per ply thickness and with an element length of 1 mm. A mesh sensitivity study was performed to investigate the trade-off between the additional computational cost associated with refining the mesh and the variation in force–displacement results and prediction of the location of the failure initiation in the foam. To balance these, the foam core mesh was refined only near the critical regions, i.e., areas with high stress gradient, such as the area under the loading roller and close to the skin–core interfaces, as well as where the experimental tests showed onset and propagation of failure. Details of the mesh for the three configurations are shown in Figure 4. In some cases, such as Figure 4b, the mesh was only further refined on one side. This asymmetric mesh definition was implemented to reduce computational time and to create a preferential location for the first failure point in the foam, matching the asymmetric failure mode observed experimentally. The mesh sensitivity study confirmed that using the smallest



elements (with dimensions  $0.3 \times 0.3$  mm) in critical regions was sufficient to accurately capture the behaviour and that further mesh refinement had no significant influence on the numerical results.

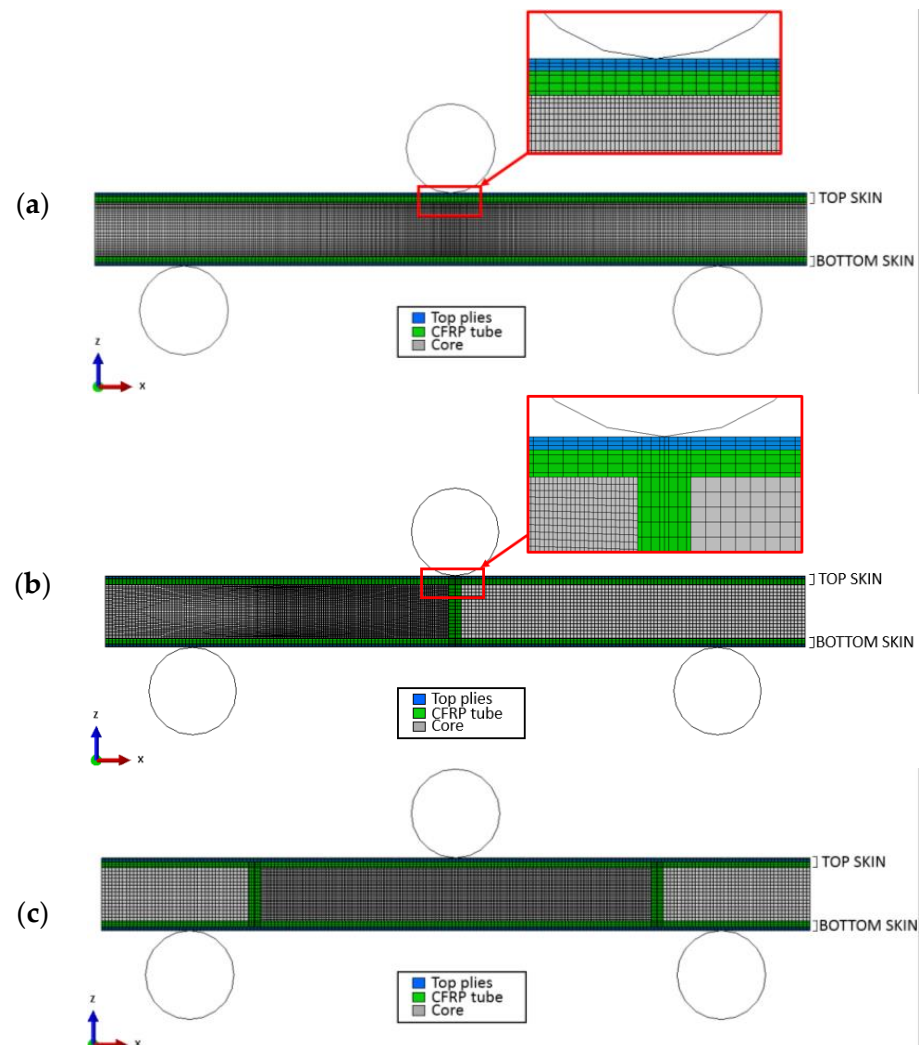


**Figure 4.** Details of the mesh for the FE model of (a) ‘Configuration 1’ (b) ‘Configuration 2’ and (c) ‘Configuration 3’ specimens.

## 4. Results and Discussion

### 4.1. Experimental Results

Typical load–displacement results and images of the development of damage for sandwich specimens with ‘Configuration 1’, ‘Configuration 2’, and ‘Configuration 3’ are shown in Figures 5–7, respectively. The load–displacement curves of all three configurations show an approximately linear elastic behaviour up to the first peak (point 1), which is the load at which the first major failure event occurred, i.e., crack development due to high shear stress levels in the foam core. For ‘Configuration 1’, a crack at an angle of  $35 \pm 5^\circ$  initiated in the foam (in between the loading and support rollers) at a load of about 4.5 kN (Point 1 in Figure 5a) and propagated at the skin–core interface, stopping, at one crack tip, underneath the top roller, and for the other crack tip, above the bottom left roller (Figure 5b image 1). This core failure occurred almost instantaneously and caused a sudden drop of the load. It should be noted that, due to the inhomogeneous strength properties of the foam (caused by the presence of defects), the crack occurred randomly on either side of the beam, with some samples showing a crack on the left half and others on the right half of the beam. A second sudden load drop (point 2 in Figure 5a) occurred once the crack at the bottom

skin–core interface propagated all the way to the edge of the sandwich beam (image 2 in Figure 5b). The load increased again after this point, reaching a value similar to that at point 1, before it experienced another drop at point 3, which corresponds to composite failure of the top skin under the loading roller where fibre crushing and breakage, as well as interlaminar cracks, were clearly visible during the experimental test (Figure 5b image 3). A final load drop (point 4 in Figure 5a) occurred as a result of sudden failure of the bottom skin (image 4 in Figure 5b).

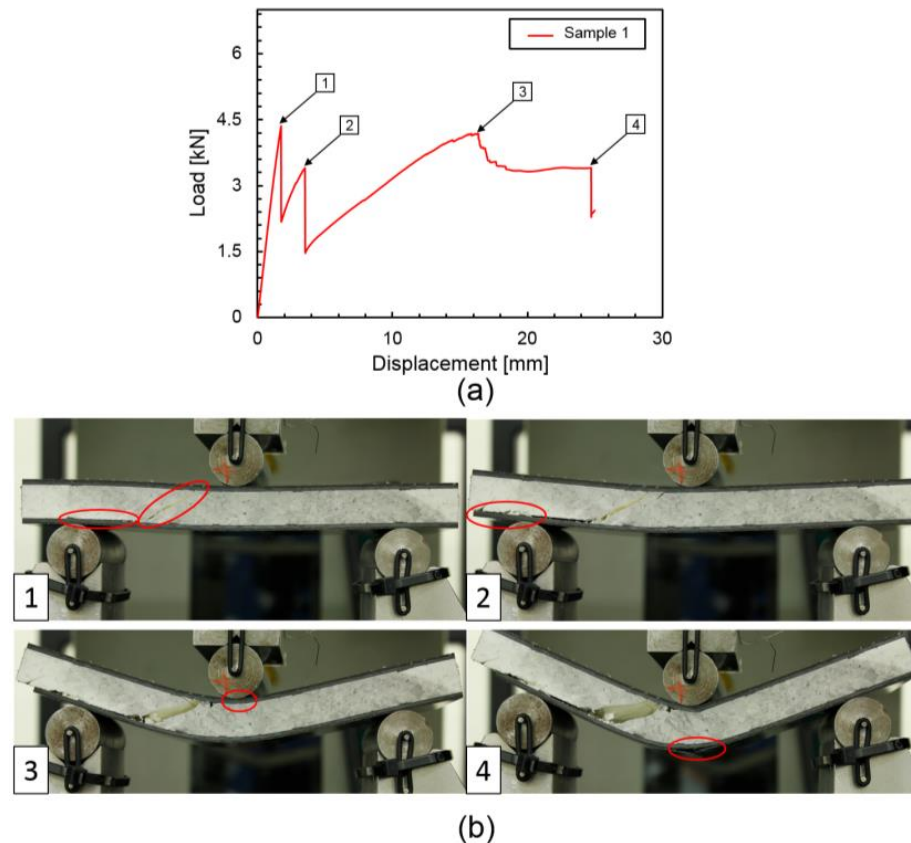
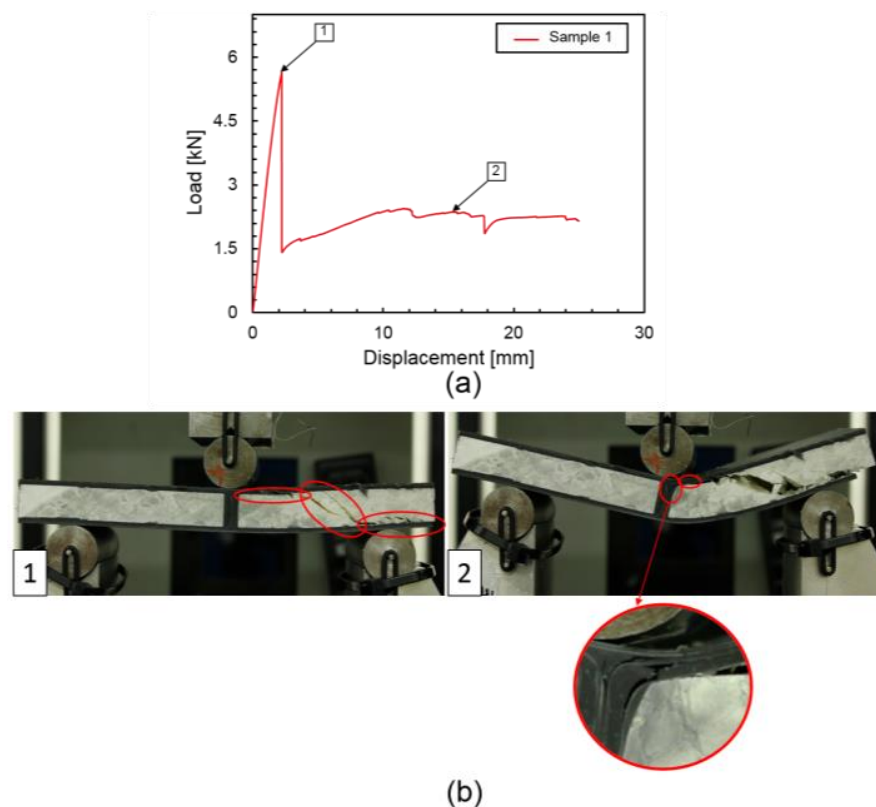


**Figure 5.** (a) Experimental load–displacement curve and (b) four images of failure development for sample with ‘Configuration 1’. The red ellipses highlight the various types of damage indicated in the text.

For ‘Configuration 2’, a major load drop was detected (point 1 in Figure 6a) when the crack developed in the foam core. Similar to ‘Configuration 1’, the crack propagated as debonding between core and top skin, ending adjacent to the central CFRP rib and between the core and bottom skin and advancing until reaching the edge of the beam. After this point, the load gradually increased, but remained at values much lower than those observed for ‘Configuration 1’ for similar displacements. Additional failure modes were observed within the top composite skin and the CFRP through-thickness rib (point 2 in Figure 6a and image 2 in Figure 6b) for this configuration, including fibre breakage, delamination, and matrix cracking in between tows and between fibres.

For ‘Configuration 3’, the first load drop in Figure 7a corresponds to the formation of a crack within the central part of the foam core between the loading roller and left support roller (image 1 in Figure 7b). The crack propagated between the core and both top and bottom skins before finally being arrested by the CFRP rib on the bottom and near the loading roller on the top core–skin interfaces. Subsequent similar crack formation and propagation occurred next in the foam between the loading roller and the right support roller, and this was responsible for the occurrence of a second load drop in the force displacement curve in Figure 7a. The cracks on the upper interface from both sides joined

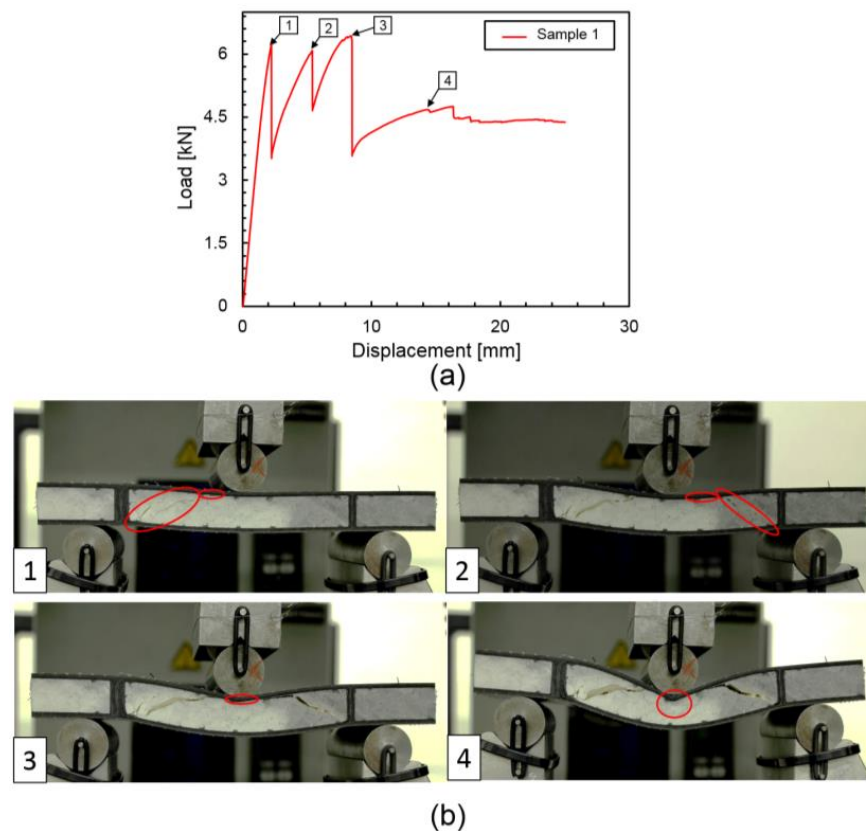
up and produced a complete skin–core debonding between the foam core and the top skin (image 3 in Figure 7b). This resulted in a third load drop in Figure 7a. It should be noted that all three load drops occurred from approximately the same value of peak load. Finally, after a gradual increase in the load after point 3, skin failure in the form of fibre breakage, delamination, and matrix damage appeared under the top roller, as indicated in image 4 in Figure 7b. While a certain degree of foam densification and crushing in the central regions of specimens in ‘Configuration 1’ and ‘Configuration 3’ was observed (i.e., areas under the loading roller), this damage mechanism was suppressed in ‘Configuration 2’, as a result of the direct positioning of the through-thickness CFRP reinforcement under the loading roller.



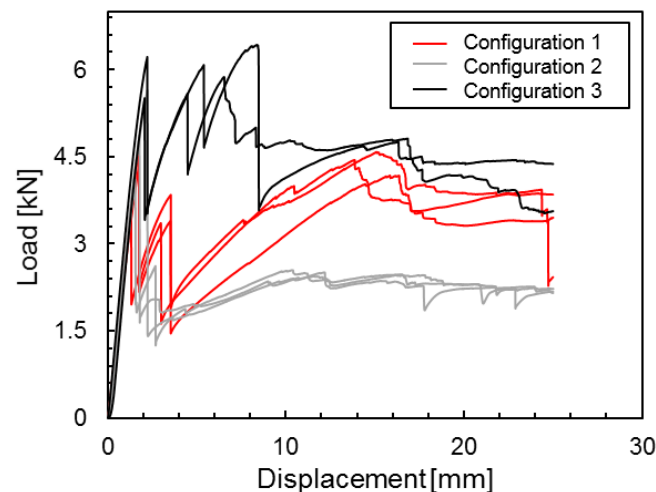
**Figure 6.** (a) Experimental load–displacement curve and (b) images of failure development for sample with ‘Configuration 2’. The red ellipses highlight the various types of damage indicated in the text.

Figure 8 shows a comparison of the experimental load–displacement curves for the three specimen configurations considered. The critical load (load at the onset of foam failure) was highest for the ‘Configuration 3’ specimens (with an average value of 5.9 kN), followed by the ‘Configuration 2’ specimens (average value of 4.8 kN) and, lastly, the ‘Configuration 1’ specimens (average value of 4.2 kN). In all the specimens, the first failure mode was foam shear failure, but the difference in the load at which it occurred was due to the variation in the shear stress and strain distributions. The best flexural performance was observed in ‘Configuration 3’, where the two ribs may have enabled a better sharing of shear across the section, reducing the shear stress in the foam, therefore delaying foam failure from occurring and resulting in a higher critical load.





**Figure 7.** (a) Experimental load–displacement curve and (b) images of failure development for sample with ‘Configuration 3’. The red ellipses highlight the various types of damage indicated in the text.



**Figure 8.** Comparison between the experimental load–displacement curves of ‘Configuration 1’, ‘Configuration 2’ and ‘Configuration 3’.

This can also be observed more clearly in Figure 9, where the DIC strain contours (shear strain  $\varepsilon_{xz}$  and normal strain  $\varepsilon_{zz}$ ) for the three different configurations are compared for an applied displacement of 1.2 mm. The shear strain field ( $\varepsilon_{xz}$ ) shows that the region experiencing high shear strain in the foam core is significantly smaller in ‘Configuration 3’ than in the other two configurations. The normal strain distribution ( $\varepsilon_{zz}$ ) in Figure 9 also indicates areas with high compressive strains under the loading roller for Configurations 1 and 3. The foam under the indenter in these configurations was free to crush and

densify in compression. This is contrary to Configuration 2, where the through-thickness rib prevented this from happening. This foam densification has a clear signature in the behaviour of the sandwich panels at higher displacements and resulted in similar responses between Configurations 1 and 3, especially at displacements greater than 8 mm.

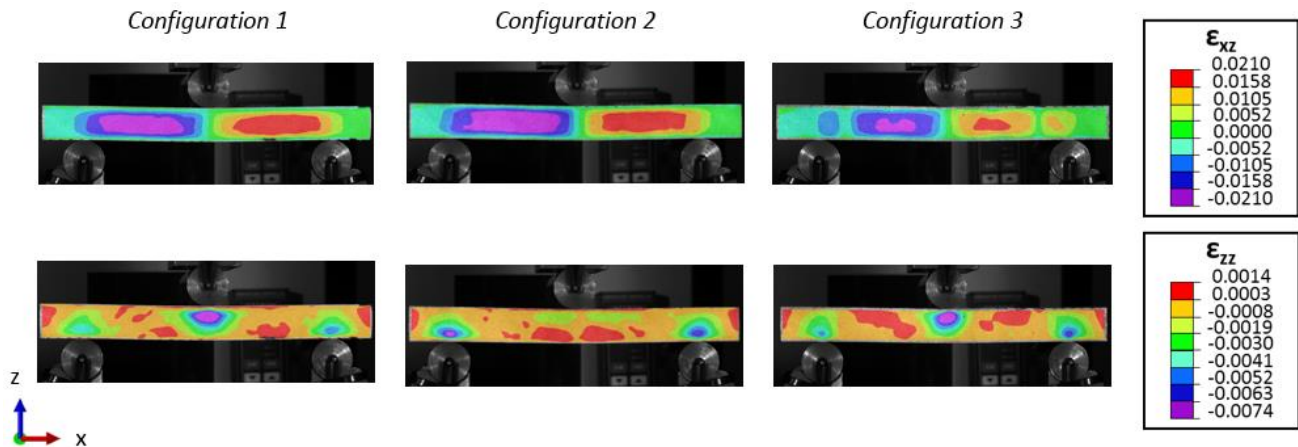


**Figure 9.** Comparison between the  $\epsilon_{xz}$  and  $\epsilon_{zz}$  strain contours of the three specimen configurations at an applied displacement of 1.2 mm.

Configuration 3 showed the highest load plateau value, as a consequence of the position of the two CFRP ribs stopping skin–core debonding from propagating; foam cracks and debonding were restricted to the central part of the sandwich beam. This is a key finding, as the positioning of the through-thickness reinforcements can be optimised in order to alter the shear stress distribution and produce delayed core failure. In addition, the ribs in ‘Configuration 3’ have restricted the debonding, foam damage, and failure in the core to a confined region, without decreasing the overall structural loading capability.

#### 4.2. Comparison with FEA

The FEA predictions for the load and displacement of all three configurations are compared with the experimental curves in Figure 10. The comparisons show good agreement between the experimental and numerical values, even at higher cross-head displacements. For ‘Configuration 1’, the FEA model predicted foam failure at an applied load of 5.1 kN, compared to the experimental value of  $4.2 \pm 0.5$  kN; for ‘Configuration 2’, the predicted value of 4.9 kN compares very well with the experimental  $4.8 \pm 0.7$  kN; for ‘Configuration 3’, the first and second load drops, corresponding to the first core shear crack and the second crack, which were predicted at 5.5 kN and 5.4 kN, respectively, and were very similar to the experimental values of  $5.9 \pm 0.4$  kN for the initial failure and  $5.8 \pm 0.3$  kN for the second crack. Figure 11 shows the FE predictions of the location and extent of foam failure for all three configurations; the numerical model captured the foam failure well at the point of first peak load for all three configurations. In all cases, a crack initiated in the core close to the bottom skin–core interface and propagated at an angle through the foam thickness; the crack subsequently produced debonding at both the top and bottom skin–core interfaces. The implemented failure criterion was able to accurately predict skin–core debonding, as well as foam failure, avoiding the need for using computationally expensive interface failure techniques, such as CZM.

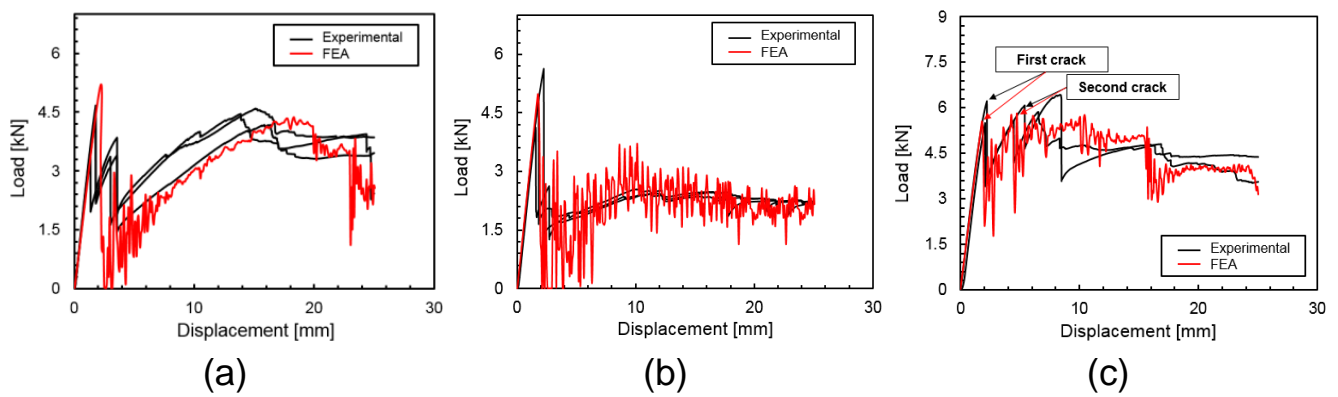
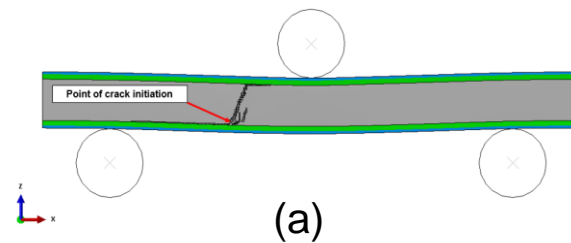


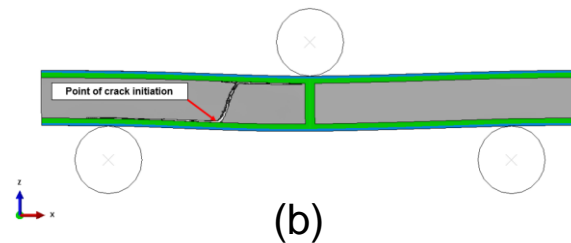
**Figure 10.** Comparison between experimental and numerical load–displacement curves for the specimens with (a) ‘Configuration 1’, (b) ‘Configuration 2’ and (c) ‘Configuration 3’.

**Configuration 1**



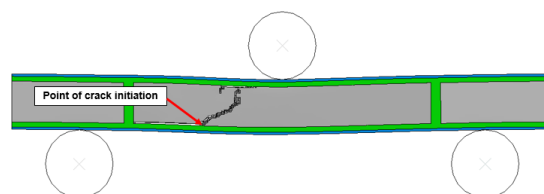
(a)

**Configuration 2**



(b)

**Configuration 3**



(c)

**Figure 11.** Deformed shape of (a) ‘Configuration 1’, (b) ‘Configuration 2’ and (c) ‘Configuration 3’ model after foam failure in shear.

The full-field strain, obtained experimentally using DIC, is compared to the FEA results at an applied displacement of 1.5 mm, before core shear failure, in Figures 12–14 for the three configurations. Figure 12 shows that a reasonable agreement was achieved between the numerical and experimental results for ‘Configuration 1’. The pre-failure

strain field revealed regions of high tensile strain in the longitudinal direction ( $\epsilon_{xx}$ ) in the foam core adjacent to the loading roller and above the two support rollers. This tensile strain region is due to the fact that the foam core material is easily deformed locally, so that, while the top skin is under longitudinal compression, a confined high tensile strain region is found in the core area below the applied load [28]. There is a good general agreement between the DIC measurements and FEA predictions for strain in the foam core (Figure 12). The FEA, however, slightly underpredicts the peak strain values for normal strains, both in the longitudinal and transverse directions (i.e.,  $\epsilon_{xx}$  and  $\epsilon_{zz}$ ) in the areas directly beneath the loading roller. The differences between FEA and DIC results are more pronounced in regions with high strain or high strain gradients. This is likely to be due to the extensive deformation of the foam (e.g., for the area under roller, as result of foam densification) and, consequently, significant distortion of the speckle pattern, beyond which the DIC algorithm became incapable of accurate tracking of individual points. The difference also can partly arise from the inaccuracy in the material model calibration of the foam, especially under complex multi-axial loading and large deformation [23].

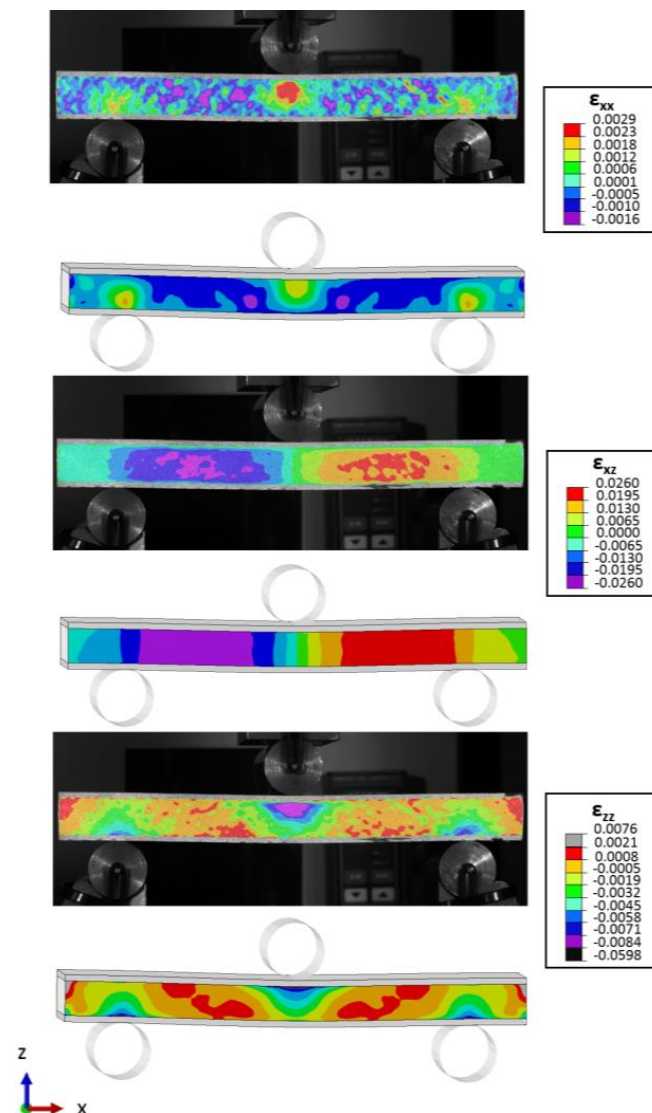


**Figure 12.** Comparison between DIC and FEA strain contours (applied displacement of 1.5 mm) for ‘Configuration 1’. For each component of strain, the experimental (DIC) result is shown first.

For ‘Configuration 2’, Figure 13 shows that the CFRP rib prevented the formation of high tensile and compressive strains in the foam region directly underneath the central loading roller in the longitudinal ( $\epsilon_{xx}$ ) and vertical ( $\epsilon_{zz}$ ) directions, respectively. The FEA overpredicts both normal and shear strains, in comparison to DIC results. The overpredicted values for normal strains are generally located around regions where the rib is connected to top and bottom skins. The high strain values in the FEA can possibly be attributed to the existence of sharp corners in the model and the associated stress concentrations. The asymmetry, with respect to the centre of the sandwich panel in the FEA shear strain field ( $\epsilon_{xz}$ ) in Figure 13, is due to the asymmetry in mesh definition between the two sides of the core (Figure 4b). As mentioned earlier, experimentally, the crack would form on either side of the specimen, due to the inhomogeneity of the foam core structure and of the loading conditions during the experiment.

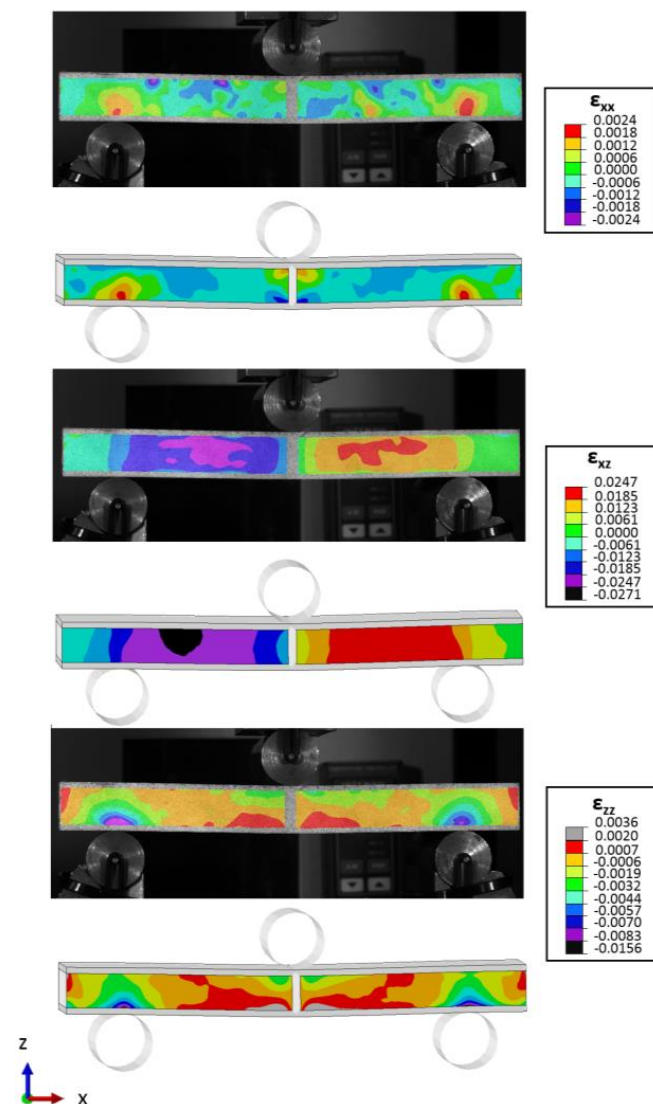


**Figure 13.** Comparison between DIC and FEA strain contours (applied displacement of 1.5 mm) for ‘Configuration 2’. For each component of strain, the experimental (DIC) result is shown first.

As with ‘Configuration 1’, the FEA model generally overpredicts peak strain values for ‘Configuration 3’, shown in Figure 14. The overpredicted values are especially apparent in the areas where localised core compression occurs (i.e., beneath the central loading roller). The maximum shear strain ( $\epsilon_{xz}$ ) value was over-predicted by the numerical model by a factor of about 1.7.



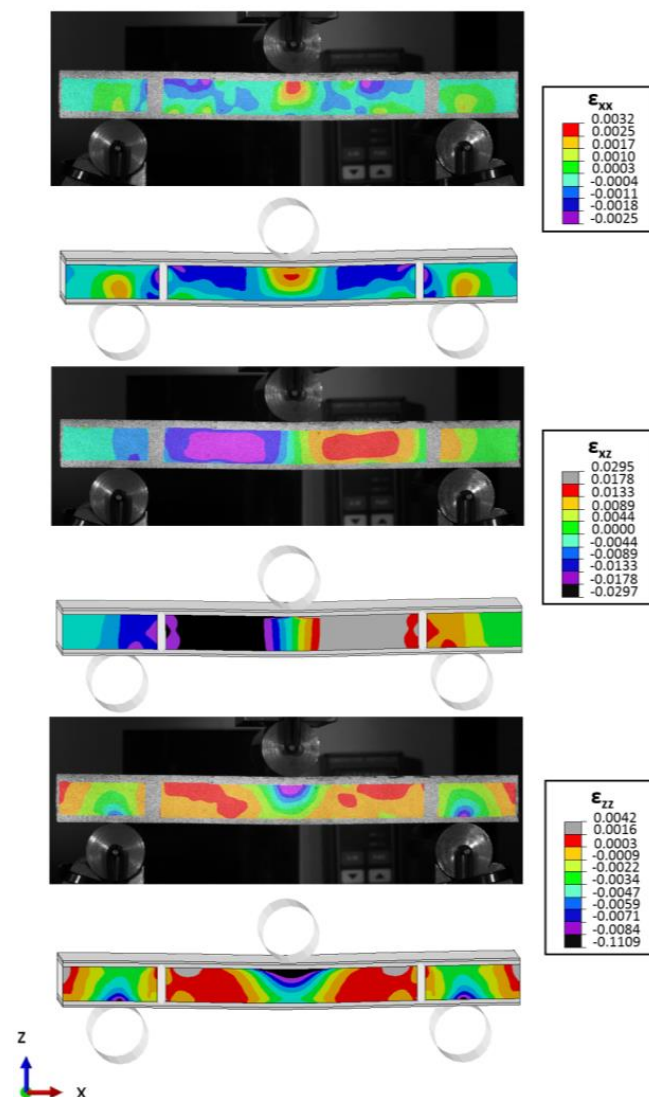


**Figure 14.** Comparison between DIC and FEA strain contours (applied displacement of 1.5 mm) for ‘Configuration 3’’. For each component of strain, the experimental (DIC) result is shown first.

In summary, the FEA models successfully capture the force–displacement behaviour of all three sandwich configurations, in terms of failure load estimation and post-failure behaviour. The models also capture the correct failure process for all configurations using a cost-effective failure modelling approach. Compared to DIC measurements, the FEA model generally has good predictions for strain distribution contours inside the foam core. Where significant localised core compression occurs, the FEA overpredicts the local strain values.

## 5. Conclusions

An experimental and numerical investigation of the flexural behaviour of polymeric foam core sandwich panels, including CFRP through-thickness rib-reinforcements, has been presented. Three specimen configurations were considered, with the aim of studying the effect of the position of the CFRP through-thickness ribs on the sandwich flexural performance. From these research findings, the following conclusions can be drawn:

- Through-thickness rib-reinforcements can be a quick and easy solution for significant improvements to the sandwich structure response to load, readily implemented during the manufacturing of sandwich structures. If appropriately tailored, the through-thickness reinforcements have the ability to maximise the panel flexural performance, as well as stabilise and control the foam failure and skin–core debonding.

- Higher critical loads at failure, and a more controlled failure process, which resulted in a higher load bearing capacity post-initial failure stage, were observed in specimens with two through-thickness ribs placed on both sides of the loading roller in a three-point bending loading configuration. This specimen configuration enabled part of the shear stresses to be transferred to the CFRP ribs, postponing core failure. In addition, this arrangement of the ribs also restricted crack propagation, skin–core debonding, and the overall panel damage in the central portion of the specimen between the two ribs.
- The developed FEA model shows good agreement with the experimental results and was successful in capturing the details of the failure process in all three configurations.
- The FEA approach used is proven to be an effective modelling approach for capturing the details of the debonding process in the composite foam structures, without the need for complex and computationally expensive interface modelling. This has a particular importance in an industrial context, as it allows larger structures to be modelled with less computational resources being required.

**Author Contributions:** Conceptualization, G.B. and A.S.; methodology, G.B., I.M., A.D.C. and S.L.O.; validation, I.M., S.L.O., A.D.C., A.S.; investigation, G.B.; data curation, G.B. and I.M.; writing—original draft preparation, G.B.; writing—review and editing, I.M., A.D.C. and S.L.O.; supervision, I.M., A.D.C., S.L.O. and A.S. All authors have read and agreed to the published version of the manuscript.

**Funding:** This work was supported by the EPSRC (award number: EP/L016788), United Kingdom, McLaren Automotive Ltd., and the University of Surrey.

**Data Availability Statement:** The data presented in this study are available on request from the corresponding author. The data are not publicly available due to sponsor’s confidentiality policy.

**Acknowledgments:** The authors would like to thank Haynes, P. and Jones, D. for assistance with aspects of the experimental work.

**Conflicts of Interest:** The content of this publication has been approved by all co-authors and institutions that have been involved in the research, with no conflict of interest, financial or otherwise.

## References

1. Carruthers, J.J.; Kettle, A.P.; Robinson, A.M. Energy absorption capability and crashworthiness of composite material structures: A review. *Appl. Mech. Rev.* **1998**, *51*, 635–649. [\[CrossRef\]](#)
2. Mamalis, A.G.; Manolacos, D.E.; Ioannidis, M.B.; Papapostolou, D.P. On the crushing response of composite sandwich panels subjected to edgewise compression: Experimental. *Compos. Struct.* **2005**, *71*, 246–257. [\[CrossRef\]](#)
3. Pfund, B. Core Installation. *Prof. Boat Build.* **2005**, *94*, 48–69.
4. Hamada, H.; Ramakrishna, S.; Nakamura, M.; Maekawa, Z.; Hull, D. Progressive crushing behaviour of glass/epoxy composite tubes with different surface treatment. *Compos. Interfaces* **1994**, *2*, 127–142. [\[CrossRef\]](#)
5. Bragagnolo, G.; Crocombe, A.D.; Ogin, S.L.; Mohagheghian, I.; Sordon, A.; Meeks, G.; Santoni, C. Investigation of skin-core debonding in sandwich structures with foam cores. *Mater. Des.* **2020**, *186*, 108312. [\[CrossRef\]](#)
6. Saeid, A.A.; Donaldson, S.L. Experimental and finite element evaluations of debonding in composite sandwich structure with core thickness variations. *Adv. Mech. Eng.* **2016**, *8*, 1–18. [\[CrossRef\]](#)
7. Warrior, N.A.; Turner, T.A.; Robitaille, F.; Rudd, C.D. The effect of interlaminar toughening strategies on the energy absorption of composite tubes. *Compos. Part A Appl. Sci. Manuf.* **2004**, *35*, 431–437. [\[CrossRef\]](#)
8. Saha, M.C.; Kabir, E.; Jeelani, S. Core/skin debond fracture toughness of S2-glass/epoxy sandwich composites with nanophased polyurethane core. In Proceedings of the 2006 SEM Annual Conference and Exposition on Experimental and Applied Mechanics 2006, Saint Louis, MO, USA, 4–7 June 2006.
9. Mamalis, A.G.; Manolacos, D.E.; Ioannidis, M.B.; Kostazos, P.K. Axial collapse of hybrid square sandwich composite tubular components with corrugated core: Experimental. *Int. J. Crashworthiness* **2000**, *5*, 315–332. [\[CrossRef\]](#)
10. Mamalis, A.G.; Manolacos, D.E.; Ioannidis, M.B.; Papapostolou, D.P.; Kostazos, P.K.; Konstantinidis, D.G. On the compression of hybrid sandwich composite panels reinforced with internal tube inserts: Experimental. *Compos. Struct.* **2002**, *56*, 191–199. [\[CrossRef\]](#)
11. Henao, A.; Carrera, M.; Miravete, A.; Castejón, L. Mechanical performance of through-thickness tufted sandwich structures. *Compos. Struct.* **2010**, *92*, 2052–2059. [\[CrossRef\]](#)

12. Jishi, H.Z.; Umer, R.; Cantwell, W.J. Skin-Core Debonding in Resin-Infused Sandwich Structures. *Polym. Compos.* **2016**, *37*, 2974–2981. [[CrossRef](#)]
13. Blok, L.G.; Kratz, J.; Lukaszewicz, D.; Hesse, S.; Ward, C.; Kassapoglou, C. Improvement of the in-plane crushing response of CFRP sandwich panels by through-thickness reinforcements. *Compos. Struct.* **2017**, *161*, 15–22. [[CrossRef](#)]
14. Glaessgen, E.H.; Reeder, J.R.; Sleight, D.W.; Wang, J.T.; Raju, I.S.; Harris, C.E. Debonding failure of sandwich-composite cryogenic fuel tank with internal core pressure. *J. Spacecr. Rockets* **2005**, *42*, 613–627. [[CrossRef](#)]
15. Toygar, M.E.; Tee, K.F.; Maleki, F.K.; Balaban, A.C. Experimental, analytical and numerical study of mechanical properties and fracture energy for composite sandwich beams. *J. Sandw. Struct. Mater.* **2019**, *21*, 1167–1189. [[CrossRef](#)]
16. Balaban, A.C.; Tee, K.F. Strain energy release rate of sandwich composite beams for different densities and geometry parameters. *Theor. Appl. Fract. Mech.* **2019**, *101*, 191–199. [[CrossRef](#)]
17. Xie, H.; Shen, C.; Fang, H.; Han, J.; Cai, W. Flexural property evaluation of web reinforced GFRP-PET foam sandwich panel: Experimental study and numerical simulation. *Compos. Part B Eng.* **2022**, *234*, 109725. [[CrossRef](#)]
18. Chen, J.; Cheng, L.; Sun, H.; Yao, X.; Fu, C.; Jiang, J. The influence of pin on the low-velocity impact performance of foam sandwich structure. *Int. J. Mech. Sci.* **2023**, *244*, 108057. [[CrossRef](#)]
19. Ghimire, S.; Chen, J. An extended cohesive damage model study of geometrical ratio effects on failure mechanisms of functionally graded sandwiches with multi-layered cores. *Compos. Struct.* **2019**, *224*, 110999. [[CrossRef](#)]
20. ASTM D3039/D3039M-17. Standard Test Method for Tensile Properties of Polymer Matrix Composite Materials. ASTM International: West Conshohocken, PA, USA, 2017; pp. 1–13.
21. ASTM D3410/D3410M-16. Standard Test Method for Compressive Properties of Polymer Matrix Composite Materials with Unsupported Gage Section by Shear. ASTM International: West Conshohocken, PA, USA, 2016; Volume 3, pp. 1–16.
22. ASTM D3518/D3518M-18. Standard Test Method for In-Plane Shear Response of Polymer Matrix Composite Materials by Tensile Test of a 45° Laminate. ASTM International: West Conshohocken, PA, USA, 2018; pp. 1–8.
23. Carranza, I.; Crocombe, A.D.; Mohagheghian, I. Characterising and modelling the mechanical behaviour of polymeric foams under complex loading. *J. Mater. Sci.* **2019**, *54*, 11328–11344. [[CrossRef](#)]
24. ASTM C393/C 393 M-06. Standard Test Method for Core Shear Properties of Sandwich Constructions by Beam. ASTM International: West Conshohocken, PA, USA, 2009; pp. 1–8.
25. Simulia, D.S. *Abaqus 2017 Documentation*; Dassault Systemes: Waltham, MA, USA, 2017.
26. Kraatz, H.A. Anwendung der Invariantentheorie zur Berechnung des dreidimensionalen Versagens- und Kriechverhaltens von geschlossenzelligen Schaumstoffen unter Einbeziehung der Mikrostruktur. Ph.D. Thesis, Martin-Luther-Universität Halle-Wittenberg, Halle, Germany, 2007.
27. Schneider, W.; Bardenheier, R. Versagenskriterien für Kunststoffe. *J. Mater. Technol.* **1975**, *6*, 269–280. [[CrossRef](#)]
28. Martins, R.; Reis, L.; Marat-mendes, R. Finite element prediction of stress-strain fields on sandwich composites. *Procedia Struct. Integr.* **2016**, *1*, 66–73. [[CrossRef](#)]

**Disclaimer/Publisher's Note:** The statements, opinions and data contained in all publications are solely those of the individual author(s) and contributor(s) and not of MDPI and/or the editor(s). MDPI and/or the editor(s) disclaim responsibility for any injury to people or property resulting from any ideas, methods, instructions or products referred to in the content.